A 3D-printed hollow microneedle-based electrochemical sensing device for in situ plant health monitoring

Reference:
Parrilla Pons Marc, Sena-Torralba Amadeo, Steijlen Annemarijn, Morais Sergi, Maquieira Ángel, De Wael Karolien.- A 3D-printed hollow microneedle-based electrochemical sensing device for in situ plant health monitoring
Biosensors and bioelectronics - ISSN 1873-4235 - 251(2024), 116131
Full text (Publisher's DOI): https://doi.org/10.1016/J.BIOS.2024.116131
To cite this reference: https://hdl.handle.net/10067/2032040151162165141

A 3D-printed hollow microneedle-based electrochemical sensing device for in situ plant health monitoring

Marc Parrilla[a,b,α,*], Amadeo Sena-Torralba[c,α], Annemarijn Steijlen[a,b], Sergi Morais[c,d], Ángel Maquieira[c,d], Karolien De Wael[a,b,*]

[a]A-Sense Lab, University of Antwerp, Groenenborgerlaan 171, 2010 Antwerp, Belgium.

[b]NANOlab Center of Excellence, University of Antwerp, Groenenborgerlaan 171, 2010 Antwerp, Belgium.

[c]Instituto Interuniversitario de Investigación de Reconocimiento Molecular y Desarrollo Tecnológico (IDM), Universitat Politècnica de València, Universitat de València, Camino de Vera s/n, 46022, Valencia, Spain.

[d]Departamento de Química, Universitat Politècnica de València, Camino de Vera s/n, 46022, Valencia, Spain.

*Correspondence: marc.parrillapons@uantwerpen.be (M. Parrilla), karolien.dewael@uantwerpen.be (K. De Wael)

[α] The authors contributed equally to this work.

Keywords: Hollow microneedles, 3D printing, Electrochemical sensors, Paper-based sampling, Plant health

Abstract

Plant health monitoring is devised as a new concept to elucidate *in situ* physiological processes. The need for increased food production to nourish the growing global population is inconsistent with the dramatic impact of climate change, which hinders crop health and exacerbates plant stress. In this context, wearable sensors play a crucial role in assessing plant stress. Herein, we present a low-cost 3D-printed hollow microneedle array (HMA) patch as a sampling device coupled with biosensors based on screen-printing technology, leading to affordable analysis of biomarkers in the plant fluid of a leaf. First, a refinement of the 3D-printing method showed a tip diameter of 25.9 ± 3.7 µm with a side hole diameter on the microneedle of 228.2 ± 18.6 µm using an affordable 3D printer (<500 EUR). Notably, the HMA patch withstanded the forces exerted by thumb pressing (i.e. 20-40 N). Subsequently, the holes of the HMA enabled the fluid extraction tested *in*

vitro and *in vivo* in plant leaves (i.e. 13.5 ± 1.1 μL). A paper-based sampling strategy adapted to the HMA allowed the collection of plant fluid. Finally, integrating the sampling device onto biosensors facilitated the *in situ* electrochemical analysis of plant health biomarkers (i.e. H_2O_2, glucose, and pH) and the electrochemical profiling of plants in five plant species. Overall, this electrochemical platform advances precise and versatile sensors for plant health monitoring. The wearable device can potentially improve precision farming practices, addressing the critical need for sustainable and resilient agriculture in changing environmental conditions.

1. Introduction

Crop health and food supply are worrying issues worldwide due to climate change and the growing population. On one side, climate change can cause plant diseases and extreme weather disasters, leading to plant stress, which dramatically influences crop production (Chaloner et al., 2021; Lesk et al., 2016; Singh et al., 2023). On the other hand, society needs to enhance agricultural production, increase crop yields, and reduce crop losses to meet the rising demand for food safety and quality (Chakraborty and Newton, 2011). These factors are driving the advancement of emerging technologies in crop management toward the detection of plant pathogens and the continuous monitoring of plant stress to ensure food security and agricultural sustainability (Giraldo et al., 2019; Li et al., 2020). Precision agriculture has risen as a crop management approach to increase crop yields and reduce costs by focusing on (near) real-time observation and analysis. Current methods mainly focus on image analysis of the whole crop (Lowenberg-Deboer and Erickson, 2019; Radoglou-Grammatikis et al., 2020). Thus, there is still the challenge of identifying localized stress in individual plants. In this direction, wearable and smart sensors can be used as scouts to gather crop information for timely decision-making (Lo Presti et al., 2023). These wearable devices have recently emerged as *in vivo* scavengers of plant health information (Lee et al., 2021). Therefore, there is a growing interest in developing technologies for real-time plant monitoring with tailored use in precision farming.

Plant health monitoring is an emerging concept that allows tracking physical and/or (bio)chemical parameters in real time on or near the plant, ideally under non-invasive or minimally invasive conditions. In this way, wearable sensors have been reported for localized microclimate and plant growth monitoring (Nassar et al., 2018). Similarly, portable sensors have been developed for plant disease control (Mohammad-Razdari et

al., 2022). A rising field of action is the continuous biochemical monitoring of plant biomarkers for the *in situ* evaluation of plant health through the real-time analysis of hormones, ions, and reactive oxygen species, among others (Coatsworth et al., 2022). In this context, electrochemical sensors aim to address continuous monitoring of (bio)chemical signals at an affordable cost due to their miniaturization capability. Therefore, wearable electrochemical sensors have a huge potential to be exploited for plant health monitoring. Recently, electrochemical sensors have been reported for the detection of hormones such as salicylic acid (Bukhamsin et al., 2022; Wang et al., 2019), indole-3-acetic acid (Chen et al., 2023; Shao et al., 2023), abscisic acid (Wang et al., 2021), other biomarkers such as nitrite and H_2O_2, (Mounesh et al., 2023b, 2023a) as well as for electrochemical fingerprinting (Yu et al., 2022). However, there are still challenges to be addressed to properly implement wearable electrochemical sensors in plant monitoring: (i) what type of wearable or implantable platform can be an effective interface between the plant and the sensor? (ii) what is the best fluid in a plant to monitor the biomarker? (iii) what biomarker correlates to abiotic or biotic stress?

The apoplast, which encompasses the intercellular space, cell walls, and xylem, is a crucial component in plants. It is responsible for transporting nutrients and water and synthesizing and distributing hormones involved in plant defense against biotic and abiotic stresses, among other functions (Farvardin et al., 2020). Therefore, the apoplast fluid can be a relevant matrix for continuous biochemical analysis (e.g. *in situ* monitoring pH) to control the plant's health status (Geilfus, 2017).

Microneedle-based arrays are a type of wearable platform used in electrochemical sensors for the minimally invasive analysis of biomarkers (Parrilla et al., 2023b) and drugs (Drăgan et al., 2023; Parrilla et al., 2023a) within the interstitial fluid of the human skin (Friedel et al., 2023). However, microneedle technology coupled with electrochemical sensors is less exploited in plant health monitoring. Therefore, we hypothesize that hollow microneedle arrays (HMA) patches can effectively access apoplast fluid by piercing a leaf, allowing subsequent biomarker analysis with an electrochemical sensor.

The fabrication of HMA devices for sample extraction is a rising field in wearable and point-of-care test biosensors (Saifullah and Faraji Rad, 2023). The most common fabrication method is micro-molding, where the molds are prepared with time-consuming and complex photolithography procedures requiring advanced cleanroom facilities (Aldawood et al., 2021). While micro-molding is a successful technique for producing

solid microneedles, the fabrication of HMA using this method is demanding due to the difficulty of creating a channel through the microneedle.

Manufacturing cost-effective HMAs for practical field deployment is critical to addressing this challenge. One aspect contributing to cost reduction is the rapid transition from laboratory-scale to mass production. Over the last decade, 3D printing has gained widespread adoption, accompanied by significant technological advancements, such as stereolithography, which has led to outstanding printing resolution at minimum costs (Dabbagh et al., 2021; Shahrubudin et al., 2019), even enabling the microengineering of microneedles (Detamornrat et al., 2022). Conversely, screen-printing technology is a well-known scalable manufacturing process for electrochemical sensors widely proved in fabricating glucose strips. Therefore, combining 3D printing and screen printing offers a scalable solution for manufacturing low-cost sensors for plant health monitoring (**Fig. 1**). Herein, we describe the fabrication of HMAs with an affordable 3D printer (<500 EUR) based on stereolithography reaching, for the first time, a tip sharpness of less than 30 µm. After a thorough characterization of the HMA, the piercing capability of the HMA was assessed. Subsequently, the HMA was evaluated for passive and active fluid extraction *in vitro* and *in vivo* using plant leaves, proving its ability to extract plant fluid. Finally, the HMA was integrated with a sensing platform based on screen-printed electrodes (SPE) for rapid and affordable *in situ* electrochemical profiling and analysis of biomarkers. The HMA and SPE were interfaced with a paper-based sampling pad that acts as a fluid collector and electrochemical cell. The device was tested for the electrochemical profiling of five plant species and detecting glucose, hydrogen peroxide, and pH in the plant leaves. The cost of an HMA/paper-based sampling device coupled to a SPE (HMAPS) is below 1 EUR, enabling the potential mass production of the devices and proving a leap forward in *in situ* plant (bio)chemical monitoring. Our device will enable the democratization of plant sensors, marking a significant advancement in plant monitoring for precision farming.

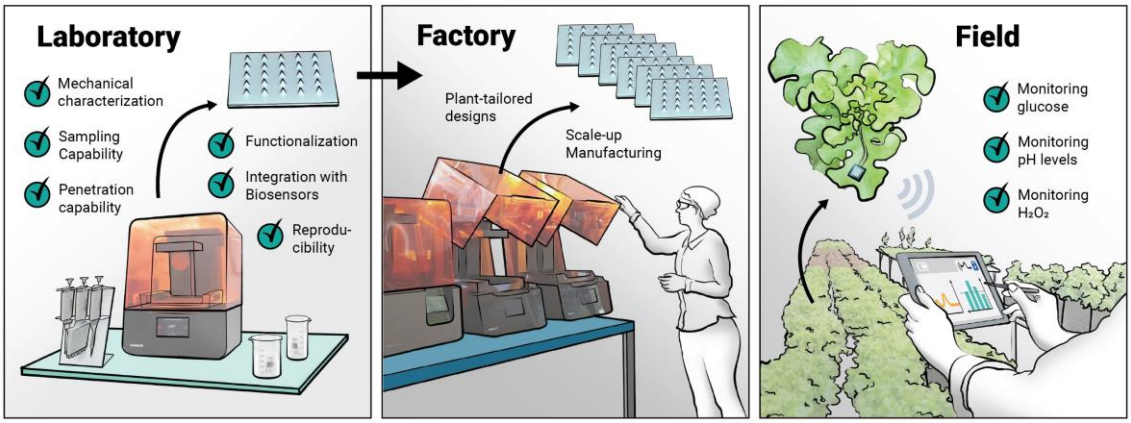

Fig. 1. Concept of laboratory design to mass-scale factory production of cost-effective hollow microneedle array (HMA) patches for fluid sampling and in situ electrochemical detection of plant biomarkers, enabled by a HMA paper-based sampling device coupled to screen-printed electrodes (HMAPS).

2. Materials and methods

The list of reagents and materials, instrumentation, and procedures, such as the fabrication of the 3D-printed HMA, characterization of the HMA insertion, SPE manufacturing, preparation of the hydrogen peroxide (H_2O_2), glucose, and pH sensors, assembly of the microneedles sensing patch with a paper-based sampling cell, among others, are included in the supplementary data.

2.1. *In vivo* electrochemical detection of plant biomarkers and plant profiling

HMAPS was used for the electrochemical detection of plant biomarkers (i.e. pH, H_2O_2, and glucose). A specific sensor was designed to analyze each biomarker and coupled to the HMA sampling device. For the plant profiling, a non-modified carbon working electrode was used. The HMAPS was inserted on the leaves of different plant species by active pressing to extract ca. 15 µL fluid to fill in the paper attached to the electrode's surface, enabling a suitable electrochemical cell. For the analysis of pH, H_2O_2, and glucose, a specific sensor was integrated into the HMAPS and followed the same sample extraction procedure.

The HMAPS, as a sampling tool, was validated by extracting the leaf fluid and measuring the analyte with an analytical method. First, a piece of the leaf is cut and inserted in a 1.5 mL tube. Thereafter, the sample was centrifuged at 1000 rpm for 5 minutes. The fluid (i.e. supernatant) is subsequently analyzed by a micro-pH meter or corresponding electrochemical sensor by depositing a sample drop on top of the sensor interfaced with a paper sampling device.

151

152 **3. Results and discussion**

153 **3.1. Printing optimization**

154 This study aims to fabricate HMAs with a simple, fast, and cost-effective 3D printing
155 method offering high batch-to-batch reproducibility and the capability to penetrate the
156 plant epidermis to extract >10 µL apoplastic fluid. To this end, the working procedure
157 involved designing the HMA structure and dimensions (**Fig. S1**). A height of 1 mm in the
158 design was selected to enable the penetration of the HMA through the external layers (i.e.
159 cuticle and epidermis) of the plant leaf available in the laboratory and allow the extraction
160 of the plant fluid where metabolic processes occur. The dimensions should vary
161 depending on the plant leaf, but this can be easily tailored by the 3D-printer. After the
162 printing process, the 3D-printed HMA was assessed through direct visual inspection to
163 identify any printing defects or artifacts that might impact surface smoothness and the
164 integrity of the hollow interior (**Fig. S2A-D**). For a more precise characterization, the
165 height, width, tip diameter, and hole diameter of the HMA were measured with the optical
166 microscope (**Fig. S2E-F**) and scanning electrochemical microscope (SEM) (**Fig. 2A-B**
167 and **Fig. S3**). Additionally, specific printing parameters, such as the UV exposure time
168 and the height layer, were evaluated. Interestingly, two HMA designs (base width of 800
169 µm and 600 µm for designs 1 and 2, respectively) were printed to interrogate the printing
170 capabilities of the 3D printer towards the smallest features in the microneedle (e.g. tip
171 diameter and hole size) (**Fig. S1** and **Fig. S2E-F**).

172 Optimizing the 3D printing method involved several key parameters. The UV exposure
173 time was a crucial factor as it significantly impacted the dimensions of the microneedles,
174 particularly their height, hole, and tip diameters. An exposure time of 1 s resulted in sub-
175 optimal curing, leading to a shorter height and a larger tip diameter than expected (**Fig.**
176 **S4**). However, a two second-exposure time generated a lower-than-expected hole
177 diameter (**Fig. S4**). As a result, an exposure time of 1.5 s was selected as the optimal
178 choice, resulting in lower deviations from the CAD (12, 3, 17, and 30% for the height,
179 width, hole, and tip diameter, respectively) (**Fig. 2C**). It is worth noting that the average
180 optimal tip diameter (i.e. 25.9 ± 3.7 µm) was only 4 µm away from the printer's resolution
181 (xy 22 µm).

182 The height layer is another parameter that influences the printing speed and, therefore,
183 the scalability potential. Hence, a height layer of 20 µm and 30 µm were compared. For
184 the latter, the tip diameter increased almost 2-fold, the hole diameter decreased 1.5-fold,

and the height decreased 1.2-fold (**Fig. S5**). These changes represented a 115%, -21%, and -18% difference from the CAD model (**Fig. 2D**), indicating dimensions lower than expected. Importantly, this variation in layer height had a minimal impact on the microneedles' width, which changed by less than 9% compared to the 20-µm layer height and exhibited a 6% difference from the CAD model. Consequently, a layer height of 20 µm was selected as the optimal choice.

The width of the microneedle is a relevant parameter to determine the overall sharpness, and thus the piercing capability, of a microneedle array. Comparing the two designs, the microneedles with a 600-µm base width displayed a 27% lower height and a 22% smaller hole diameter than expected (**Fig. 2E**). The tip diameter was only slightly smaller (23.6 ± 1.8 µm), with no significant difference from the tip diameter of the microneedles with an 800-µm base width. The printed microneedles achieved the expected width in both designs, with less than a 6% difference from the CAD model.

After confirming that the printed HMA closely matched the CAD dimensions, we assessed the printing reproducibility using the Design 1 HMA. Several aspects were measured, such as the distance between microneedles in the array and the microneedles' height, width, hole, and tip diameter, using the optical microscope and SEM. We compared the dimensions of 5 different microneedles within the same patch (**Table S1**), between different patches (**Table S2**), and across several batches (**Table S3**). Following the evaluation of 100 microneedles, we determined that the relative standard deviation (RSD) for the distance between microneedles, microneedles' height, and hole diameter was less than 3%, while the RSD for the tip diameter was 10% **(Fig. 2F).** These results are remarkable, particularly considering the fabrication method's simplicity, speed, and cost-effectiveness.

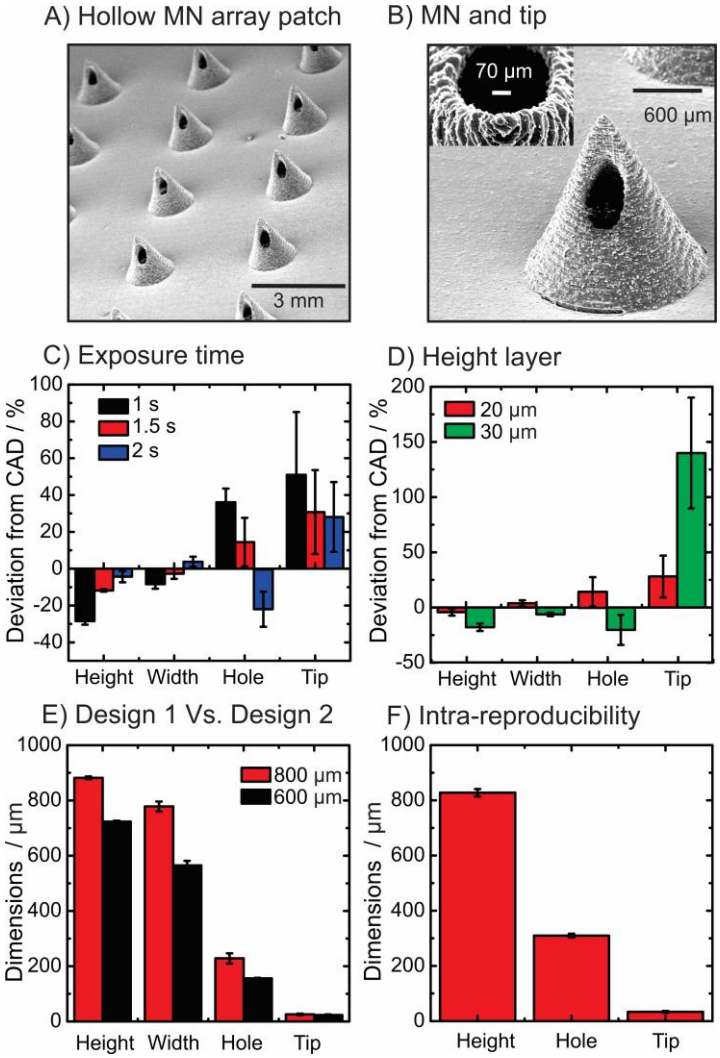

Fig. 2. Design and evaluation of the 3D-printing capabilities: A) SEM image of the HMA patch. B) SEM image of a hollow microneedle, inset from the top view of a hollow microneedle, showing the hole and tip sharpness. Optimization of the C) exposure time and D) height layer on the printing capability of a 3D-printed HMA patch (N=3). E) Comparison of the dimensions between Design 1 (800 µm base diameter) and Design 2 (600 µm base diameter). F) Intra-batch reproducibility of the 3D-printing method (N=5).

3.2. Mechanical characterization

The paramount feature of the HMA patch lies in its capacity to penetrate a substrate while retaining its structural integrity. Therefore, the subsequent phase of our research focused on evaluating the mechanical robustness and post-piercing resilience of the 3D-printed HMA. Parafilm test was employed as an *in vitro* model for assessing the HMA's insertion capabilities (Larrañeta et al., 2014). Employing a universal testing machine, a range of forces (specifically, 20, 30, and 40 N) were applied to complete the insertion test. These

force levels align with the average forces reported during a 30-second thumb-pressing insertion (Larrañeta et al., 2014).

The mechanical characterization of the HMA was performed on Design 1 and Design 2 to evaluate the robustness of the HMAs, an essential parameter in microneedle devices. **Fig. S6A** depicts the displacement of the HMA patch by applying the forces. The displacement represents the insertion of the microneedles into the Parafilm layers in millimeters. Forces of 30 N and 40 N yielded similar penetration depth, specifically 798 µm and 890 µm, respectively, for Design 1, compared to 20 N, which resulted in a penetration depth of 596 µm. **Fig. S6B** illustrates the displacement corresponding to a penetration depth of 639 µm, 778 µm, and 725 µm for 20, 30, and 40 N, respectively, for Design 2. It is worth noting that the reduction in penetration depth for Design 2, when applying a force of 40 N, already suggests potential microneedle deformation.

The Parafilm test consists of piercing the HMA into a ten-layer folded Parafilm. **Fig. S7** shows the images of each pierced Parafilm layer at different applied forces using Design 1. **Fig. S8** depicts the results obtained in the Parafilm test employing Design 2. The penetration depth through the Parafilm test was determined by counting the holes at each layer (each layer accounts for 127 µm thickness), as shown in **Fig. 3A** for Design 1 and **Fig. S9A** for Design 2. Design 1 showed optimal insertion performance when forces of 30 and 40 N were applied. In contrast, Design 2 displayed optimal insertion performance with 40 N. Both designs penetrated over 500 µm in almost 100% of the tested microneedles. These results are remarkably favorable for a 3D-printed HMA compared to previously reported 3D-printed HMA patches (Economidou et al., 2021; Mathew et al., 2021; Uddin et al., 2020; Xenikakis et al., 2019). This outstanding performance can be attributed to the advanced printing capabilities of the 3D printer, which offers a xy resolution of 22 µm. The penetration depth into the Parafilm layers was also assessed by performing a transversal cut. **Fig. 3B** shows the measured depth by light microscopy corresponding to the images in **Fig. 3C**. Higher penetration values were obtained (i.e. up to 640.9±18.3 µm for 30 N), showing the excellent piercing capability of the 3D-printed HMA.

The deformation of the HMAs was subsequently evaluated by light microscopy. **Fig. 3D** illustrates the images before and after the Parafilm test for Design 1. **Fig. S9B** shows the corresponding images before and after the Parafilm test for Design 2. Interestingly, no evidence of deformation was observed for Design 1. In contrast, Design 2 displayed a significant tip bending after the test. More specifically, the height reduction and tip

deformation were assessed in both Designs. As depicted in **Fig. 3E,** a minor decrease in the microneedle height was observed when applying 20 N. A higher reduction occurred when applying 30 N, and a significant reduction, particularly in Design 2, was observed when a force of 40 N was applied (i.e. 247.2 ± 29.8 µm).

Similarly, tip deformation was most pronounced for Design 2 at 40 N (i.e. 186.5 ± 17.2 µm) (**Fig. 3F**). This deformation can be attributed to the tip bending downwards as this design has a smaller structural profile and is more fragile. Notably, despite a slight height reduction and tip deformation observed for Design 1 after applying a force of 40 N (i.e. 63.5 ± 6.8 µm and 28.8 ± 6.1 µm, respectively), the microneedles did not display significant deformation, demonstrating the suitability of this design for future applications. Based on these results, only Design 1 was selected as the optimal one to assess the extraction capabilities of the 3D-printed HMA.

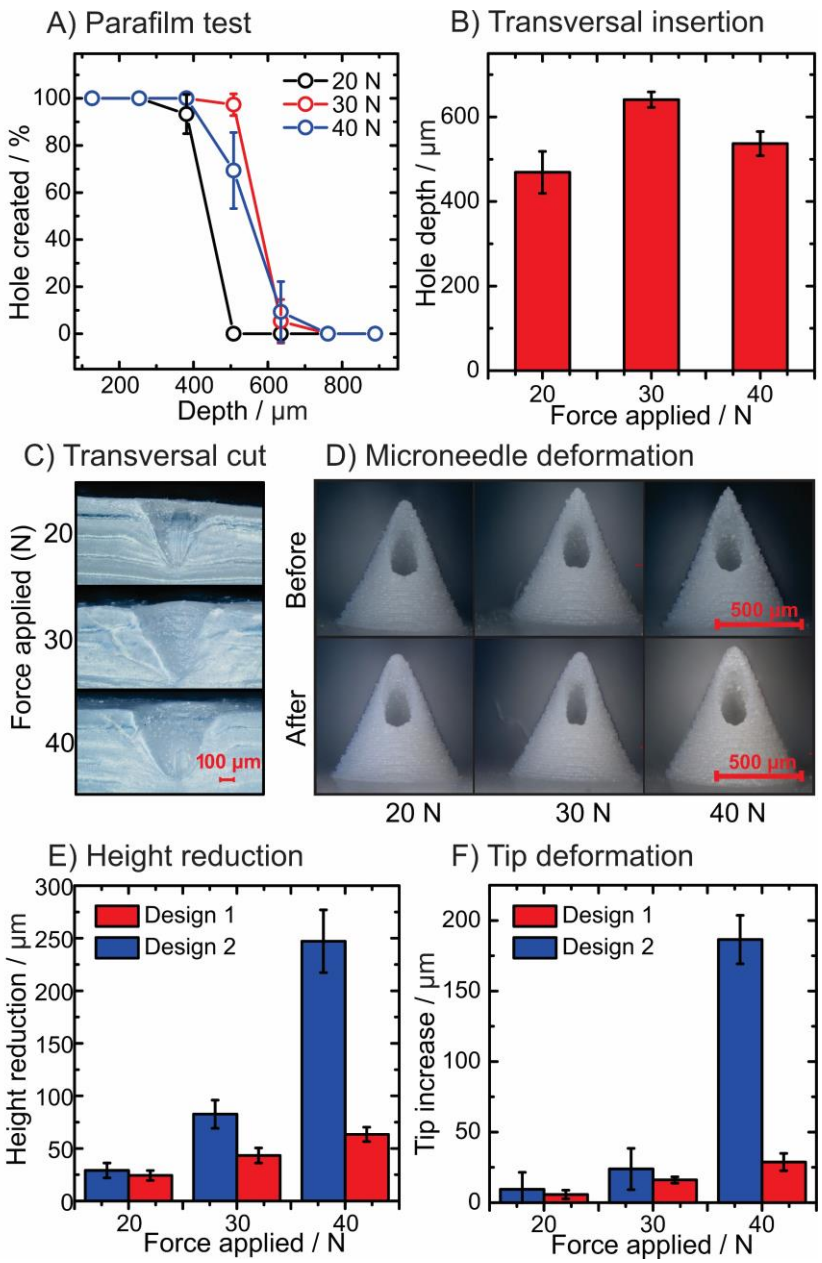

Fig. 3. Evaluation of the mechanical strength and piercing capabilities using a universal testing machine on the Parafilm layers by applying forces of 20, 30, and 40 N. A) Percentage of holes created by the HMA patches observed after the Parafilm insertion test. B) Hole depth using the transversal cut test. All experiments were measured in triplicate in a single HMA patch. C) Transversal cut of the Parafilm layers. D) Optical microscope images of the hollow microneedle from Design 1 before and after performing the mechanical test. Evaluation of the deformation after the mechanical test in Parafilm, E) height reduction and F) tip deformation.

3.3. Evaluation of the extraction capabilities

3.3.1. Evaluation of the hydrophilic properties of the HMA

The primary aim of HMA is to serve as a sampling tool for extracting extracellular fluids in plants. The HMA was initially evaluated in a controlled solution setting to assess its efficacy. For visual interpretation, an aqueous solution containing 0.1 mg mL^{-1} of methylene blue was employed to determine the fluid uptake capacity of the HMA (see **Fig. S10**). The HMA is fabricated from a polymeric material with low hydrophilicity, so different assay conditions were also assessed. These conditions included using 5 mM Tween-20, 5 mM sodium dodecyl sulfate (SDS), 5 mM lactic acid, and 0.5% chitosan (CHI). **Fig. S10A** shows the reverse side of the patch following its placement on top of a 75 µL droplet solution for 120 seconds. **Fig. S10B** shows the collected fluid by the HMAs after 120 seconds. As expected, the HMAs with the surfactants Tween-20 and SDS displayed the highest fluid uptake due to their enhanced surface hydrophilicity. Conversely, the other assay conditions made HMAs fill only the cavities within the patch. Consequently, the subsequent tests exclusively considered the surfactant-modified HMAs.

A preliminary filter paper test was conducted to assess the performance of the paper-based sampling device (**Fig. S11**). **Fig. S11A** illustrates the progression of fluid uptake through the cavities toward the paper during a 200-second interval. **Fig. S11B** showcases the rapid color change of the filter paper, quantified by the change in intensity. The HMA modified with surfactants demonstrated nearly instant wetting of the paper after 25 seconds, in contrast to the non-modified HMA (i.e. water), which is not hydrophilic enough to bring the solution in contact with the paper.

3.3.2. *In vitro* passive extraction of fluid by HMA

Since the extracellular fluid is usually embedded within a matrix of cells, employing a fluid model falls short of replicating real-life conditions accurately. Hydrogels can be used to better mimic an *in vitro* scenario. This study employed a 4% agarose gel to test fluid extraction capability from a matrix. In this test, the paper piece was first soaked with $CoCl_2$, which changes color from blue to pink and white upon contact with water molecules (Zhu et al., 2022). This method was chosen because it provided a more consistent color change than methylene blue-soaked paper (**Fig S11A**).

Fig. 4A shows the results of a passive fluid extraction test on agarose hydrogel over 300 s, which involved piercing the HMA into the hydrogel without applying pressure. **Fig. 4B** depicts the color change, shifting from blue to pink-white, during the insertion of the HMA paper sampling device (HMAP). The unmodified HMA (i.e. using water) already

exhibited a slight color change with an increasing intensity, which might be attributed to the humidity from the channels on the HMA filled with solution from the agarose.

Remarkably, adding surfactants resulted in a rapid color change, particularly after 60 s, with a plateau observed at 300 s. Therefore, surfactants clearly show an effect on fluid uptake. The type of surfactant used did not lead to a significant difference during the passive fluid uptake. A calibration curve was generated to quantify the volume of fluid that the device could uptake using the $CoCl_2$-modified paper (**Fig. S12A**). This calibration curve demonstrated a linear relationship between 0.5 µL and 2.0 µL (**Fig. S12B**). Given that the HMAP exhibited an intensity of 0.8 at 300 seconds, surpassing the linearity threshold (i.e. 0.7 with 2.0 µL), it can be inferred that the HMAP can passively extract more than 2.0 µL of solution from the agarose hydrogel in 5 min.

3.3.3. *In vivo* fluid extraction in plant leaves

The HMAP aims to extract apoplast fluid from a plant leaf as a proof of concept. The plant leaf was selected because of its high surface and planar area which allows a successful insertion of the HMAP. Hence, the HMAP was tested for passive fluid extraction by piercing a leaf of *Pilea peperomioides*. **Fig. 4C** shows the time frames after the insertion of the HMAP on the leaf during 300 s. **Fig. 4D** illustrates the corresponding color change due to the potential fluid uptake from the leaf. In this case, Tween-20 was the optimal modifier exhibiting faster fluid uptake, reaching a plateau at 300 s with almost 2 µL fluid uptake. The unmodified HMA displayed a solution uptake similar to that of the agarose test (i.e. 0.4 intensity). **Fig. 4E** illustrates a cross-sectional view of a microneedle inserted in a leaf (left image) and the resulting hole in the leaf after removing the HMAP (right image), demonstrating a minimal impact on the leaf´s integrity.

The goal of the HMAP is to extract a sufficient volume of apoplast fluid from a plant leaf to saturate the filter paper and enable proper contact with the sensor for electrochemical analysis. Unfortunately, 2 µL is not enough volume to enable a full electrochemical cell in contact with the SPE for accurate electrochemical analysis. Thus, an active fluid extraction by keeping the thumb pressed on the leaf was pursued allowing to extract higher volume of fluid. **Fig. 4F** illustrates the collected volume after 30 seconds of active thumb pressing of the HMAP on a plant leaf. In this experiment, all HMA patches showed similar extraction capabilities. HMA_{Tween} patches extracted 18.0 ± 3.3 µL, HMA_{Water} extracted 13.5 ± 1.1 µL, and HMA_{SDS} extracted 12.6 ± 1.1 µL. In all cases, the volume extracted through active pressing was suitable to saturate the HMAP and enable an electrochemical cell for the biosensor.

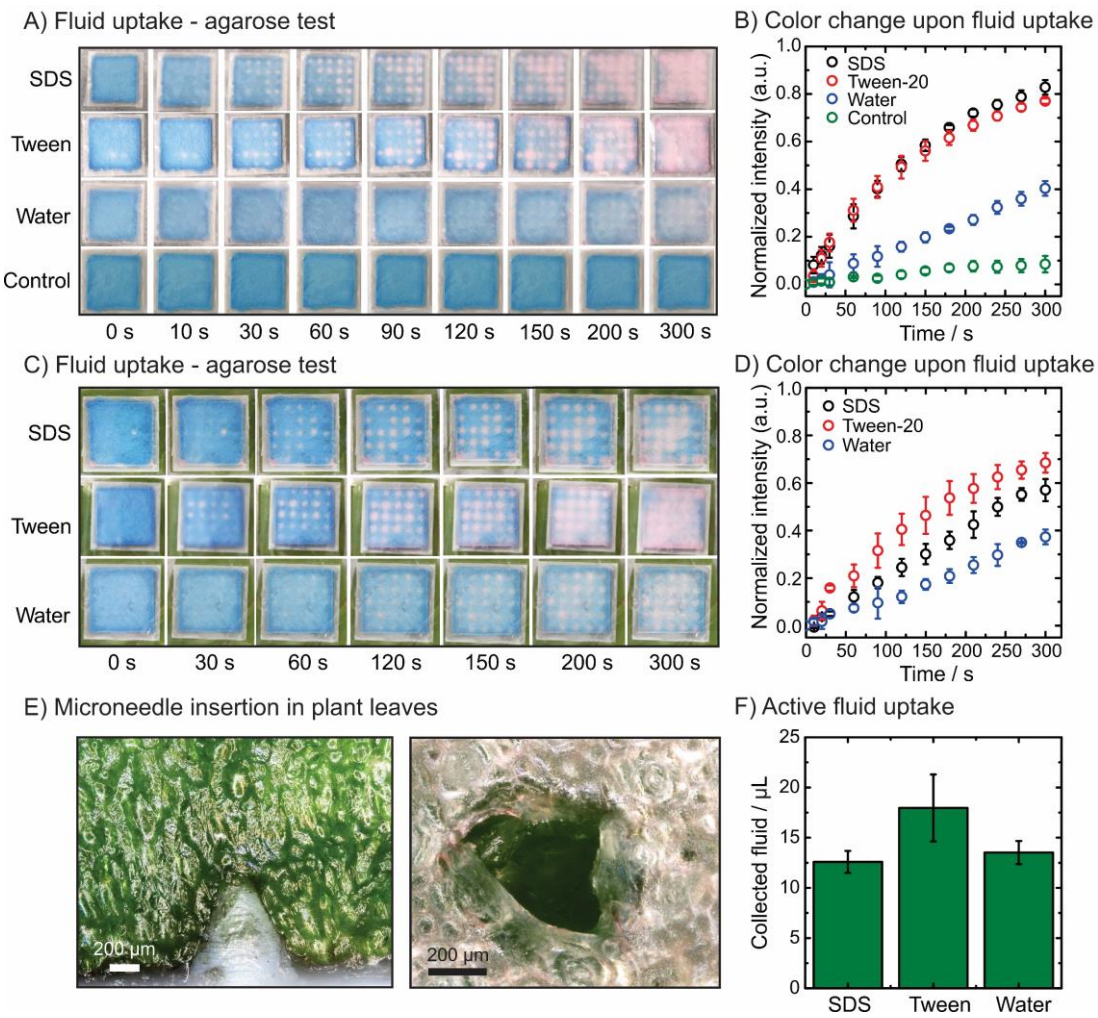

Fig. 4. Assessment of the fluid uptake by the HMA patch sampling method using different modifiers. A) Images of the passive fluid uptake on an in vitro model (i.e. agarose hydrogel) by the HMA patch on the paper-based sampling coated with $CoCl_2$, and B) quantitative analysis of the color changes from the images. C) Images of the passive fluid uptake on an in vivo model (i.e. Pilea peperomioides leaves) by the HMA patch on the paper-based sampling coated with $CoCl_2$, and D) quantitative analysis of the color changes from the images. The RGB histogram plugin in ImageJ performs the color change quantification. E) Image of a transversal cut of a plant leaf inserted with a HMA patch (left) and image of the hole after removal of the HMA patch in a plant leaf. F) Quantification of the active fluid uptake after insertion and pressing of the modified and non-modified HMA patch into a plant leaf. All assays were performed in triplicate.

3.4. Electrochemical sensing applications for plant health monitoring

Screen-printing technology has enabled the democratization of electrochemical sensors by providing scalable and affordable fabrication of SPE. Integrating an SPE with an

365 HMAP as a sampling device can yield an affordable point-of-need test for *in situ* plant
366 monitoring. **Fig. 5A** displays the construction of the HMAPS consisting of the HMA, a
367 filter paper embedded in a spacer, and the SPE. The spacer is a double-sided adhesive
368 that allows the HMA to stick to the SPE while keeping a paper-based electrochemical cell
369 as an interface. The paper-based cell is filled with a smaller volume, which is crucial
370 when dealing with low extraction volumes. It also traps biomacromolecules that might
371 passivate the electrode's surface while enabling the diffusion of small molecules toward
372 the surface. To test the ability of the HMAPS for the detection of different plant
373 biomarkers, the SPE was modified with Prussian blue (PB), PB with glucose oxidase
374 (GOx), and polyaniline (PANI) for the detection of H_2O_2, glucose, and pH, respectively.
375 H_2O_2 and pH are reporters of the stress level, and glucose is used as a metabolic biomarker
376 (Coatsworth et al., 2022; Lo Presti et al., 2023). Moreover, unmodified SPEs were used
377 on the HMAPS for voltammetric plant profiling. Notice that the full analytical
378 characterization of the H_2O_2, glucose, and pH (bio)sensors has been previously reported
379 by the authors and the same fabrication methodology is employed in this manuscript
380 (Parrilla et al., 2022a; Steijlen et al., 2024).
381 The evaluation of the paper-based sampling strategy was conducted. The HMAPS,
382 without any modification of the SPE, was tested in buffer and potassium ferricyanide
383 solution (i.e. 5 mM) to assess the impact of the paper sampling on the electrochemical
384 response. **Fig. S13A** shows the cyclic voltammograms (CV) of ferricyanide obtained
385 through two methods: the direct drop (80 µL) and the paper-based interface (15 µL). In
386 both tests, the typical electrochemical behavior, characterized by the appearance of the
387 two redox peaks from ferricyanide, was observed using a graphite-based SPE. The use of
388 the paper-based sampling resulted in a 23.5% reduction in the current on the anodic peak
389 (I_p). This effect can be attributed to a potential decrease in the electroactive area, likely
390 due to interactions between some cellulose fibers and the electrode's surface. Despite the
391 reduction in current, it is worth noting that the peak potential (E_p) remained unchanged,
392 which is crucial for maintaining the integrity of the electrochemical profiling.
393 **Fig. S13B** depicts a repeatability test of 5 mM ferricyanide in the same electrode,
394 demonstrating the viability of the paper-based sampling on the SPE. First, the
395 electrochemical profile from the extracted fluid (without the HMAP) from the leaf of
396 *Pilea peperomioides* was studied to evaluate the feasibility of the electrochemical
397 profiling. **Fig. S13C** shows the CVs of fluid extracted by crushing the leaf (curve 2) and
398 by centrifugating the leaf (curve 3). The obtained electrochemical profile depicted a broad

oxidation process at 0.7 V without successful profiling. However, when the paper interface was introduced on the surface of the SPE, an enriched electrochemical profile was unraveled, showing anodic and cathodic processes (**Fig. S13D**, curve 4). This effect can be explained by the paper's filtration step, which removes protein and other biomacromolecules that can be adsorbed at the surface of the SPE and cause biofouling. Importantly, we study the exertion of pressure on the paper to evaluate the effect on the electrochemical profile. Indeed, the oxidation peaks overlapped potentially due to increased resistance in the media (curve 5). Thus, the HMAPS was designed to prevent the paper from compressing during the tests by introducing a spacer in the paper cell. Finally, the positive filtration impact of the paper was assessed by extracting the plant fluid through the HMAP, centrifuging, and analyzing at the SPE (curve 6), depicting a well-defined electrochemical profile. Once the electrochemical profile was determined using the HMAPS, a reproducibility test was performed using three different HMAPS (**Fig. S13E**). The CVs showed three pronounced redox peaks (i.e. two anodic and one cathodic), proving the system's ability for plant profiling.

Fig. 5B depicts five electrochemical profiles obtained from five different plants. Interestingly, the electrochemical profiles exhibited broad differences in the redox peaks and different ratios of peak intensities, meaning that different compounds and concentrations are involved in the profiling. Square-wave voltammetry (SWV) increased the peak resolution and separation in the electrochemical profiling. This technique has been widely used for the electrochemical profiling of electroactive compounds (Parrilla et al., 2022b). **Fig. 5C** and **Fig. 5D** show the anodic and cathodic scans for each plant, respectively. Similar results were obtained with CV, although SWV increased the profiling resolution at specific $E_{p,}$ thus enabling an easy comparison of the plant profiles. **Fig. 5E** shows three profiles obtained by SWV by three different HMAPS in the same plant leaf (i.e. *Pilea pepermioides*). Three redox peaks characterize the electrochemical profile of *Pilea peperomioides*, i.e. E_{ox1} = 0.392 ± 0.015 V; E_{ox2} = 0.747 ± 0.009 V; and E_{red1} = 0.060 ± 0.014 V. The impact of leaf health on the electrochemical profile was studied in three states: green leaves, transitioning from green to yellowish leaves, and entirely yellow leaves. A change in the redox peak potentials was observed when analyzing the apoplast fluid of the yellowish leaves (**Fig. 5F**). E_{ox1} and E_{ox2} shift toward higher potentials (E_{ox1}=0.504± 0.001V; E_{ox2}= 0.795± 0.003V) and E_{red1} shifts toward more negative potentials (E_{red1}=0.016± 0.003V). It is suggested that these changes in the

E_p can be produced by a change in the pH of the apoplast (Geilfus, 2017), which in turn changes the electrochemical profile.

The next step was to evaluate the ability of the HMAPS to *in situ* analyze relevant indicators for plant health monitoring. In the apoplast fluid, H_2O_2, glucose, and pH are significant indicators of plant health (Coatsworth et al., 2022). After the functionalization of the SPE (see details of the fabrication and characterization in the supplementary material), the biosensors were subsequently assessed by piercing the leaves of different plant species (i.e. Plant 1 - *Pilea pepermioides* and Plant 4 - *Echeveria Raindrops*) using the HMAPS configuration. In parallel, plant leaf fluid was extracted by standard methods (i.e. centrifugation) and analyzed with a biosensor without the HMAPS approach. **Fig. 5G** shows the chronoamperograms for H_2O_2 detection gathered during the calibration curve from 10 to 100 µM and the analysis of the extracted fluid using centrifugation and HMAPS of Plant 4. **Fig. S14A** displays the corresponding calibration curve showing excellent linearity, which falls in the physiological range of H_2O_2 in plants (i.e. 10–100 µM) (Giraldo et al., 2019; Lima et al., 2018) and a slope of -3.2 nA μM^{-1}. **Fig. 5H** illustrates the corresponding concentrations of the plant fluid extracted by the two methods showing a concentration of 111.7 ± 4.3 µM for Plant 1 and 45.0 ± 1.6 µM for Plant 4 using HMAPS. The analysis of H_2O_2 in Plant 1 exhibited a difference of 40.5 ± 1.7 % between methods in the H_2O_2 concentration due to a potential delay in the analysis of the samples. In contrast, the levels of H_2O_2 in the leaf of Plant 4 were similar between both methods (12.5 ± 0.9 % difference between methods). However, an RSD of 1.6-2.3 % between different biosensors/HMAPS proves the reliability of the electrochemical approach. It is thus highly relevant to develop a reliable extraction method of the apoplast fluid in the laboratory to validate the H_2O_2 levels properly.

Similarly, **Fig. 5I** illustrates the chronoamperograms for glucose detection obtained during the calibration curve from 50 to 1500 µM and the analysis of the extracted fluid using centrifugation and HMAPS of Plant 1. **Fig. S14B** exhibits the corresponding calibration curve with the linearity falling in the physiological range of glucose in plants (i.e. 0.1–1000 µM) (Giraldo et al., 2019) and a slope of -0.6 nA μM^{-1}. **Fig. 5J** shows the corresponding concentrations of the plant fluid extracted by the two methods showing a concentration of 544.4 ± 16.2 µM for Plant 1 and 1619.6 ± 247.1 µM for Plant 4 using HMAPS. A difference of 3.6 ± 3.2 % and 5.7 ± 5.6 % between the extracted fluid and the HMASP was obtained during the analysis of Plant 1 and Plant 4, respectively. Finally, the pH of the apoplast fluid of four plants was measured (**Fig. 5K**). The pH sensor was

466 previously analytically characterized by performing a reversibility test (**Fig. S14C**)
467 exhibiting a linear range between pH5 and pH8 with a slope of -71.0 mV pH^{-1} (**Fig. S14D**)
468 corresponding to a suitable indicator range for plant health events (i.e. pH 5.2 – pH 8.4)
469 (Giraldo et al., 2019). The pH sensor provided values from 5.2 to 6.1, with Plant 4 and
470 Plant 3 being the most (i.e. pH 5.2 ± 0.1) and least acidic (i.e. pH 6.1 ± 0.2), respectively.
471 These values align with regular pH levels found in plants (Geilfus, 2017).
472 Notably, various plants displayed varying levels of H_2O_2, glucose, and slightly distinct
473 pH values in the apoplast fluid, indicating the significant variability in physiological
474 processes within plants. The method presented in this study, HMAPS, serves as a proof
475 of concept for the rapid, *in situ* detection of plant biomarkers, requiring minimal user
476 intervention. Nevertheless, the investigation of the correlation between the insertion of
477 the HMAPS and the biomarkers' level needs to be performed to ensure that the
478 mechanical action of disrupting the external layers of the leaf (i.e. cuticle and epidermis)
479 does not affect the composition of the biomarkers for proper decision-making processes.
480 As the HMAPS can be also applied for in-field analysis, a temperature variation algorithm
481 would be needed to account for the electrochemical signal variation, and thus minimize
482 analytical errors.
483

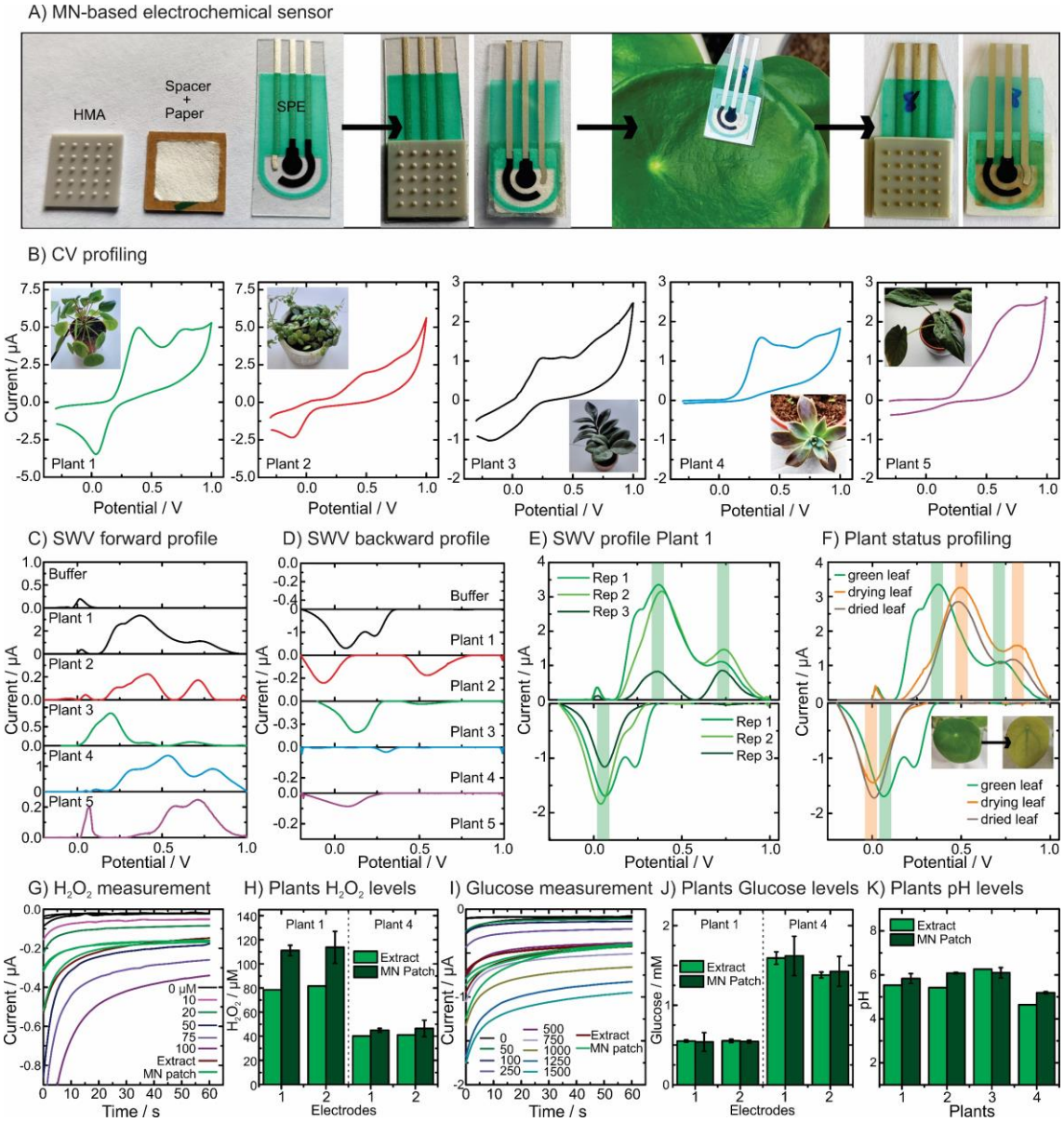

Fig. 5. In situ (bio)chemical plant health monitoring by the HMA/paper-based sampling device coupled to an electrochemical sensor (HMAPS). A) Illustration of the construction of the HMAPS showing the elements and the in-field testing. B) Evaluation of the capacity of the HMAPS for plant profiling by cyclic voltammetry (CV) in five different plant species. Electrochemical profiling of the five plant species by square-wave voltammetry (SWV) using C) the anodic and D) the cathodic profiling. E) Repeatability test of the electrochemical profiling on the leaves of Plant 1 (N=3). F) Evaluation of the electrochemical profiling on different healthy leaves of Plant 1 (green, yellow, and dried leaves). G) Chronoamperograms from the H_2O_2 sensor of standards and plant extracts by conventional method and the HMAPS system obtained during Plant 4 analysis. H) Comparison of the H_2O_2 levels found in Plant 1 and Plant 4 extracts using conventional and HMAPS methods. I) Chronoamperograms from the glucose biosensor of standards

and plant extracts by conventional extraction method and the HMAPS system obtained during Plant 1 analysis. H) Comparison of the glucose levels found in Plant 1 and Plant 4 in the extracts using conventional and HMAPS methods. K) pH analysis of Plant 1, 2, 3, and 4 extracts using a commercial micro glass pH meter and the HMAPS system modified with a PANI sensor (N=3).

4. Conclusion

We have developed a low-cost 3D-printed hollow microneedle array coupled with a screen-printed electrode (HMAPS) for the electrochemical health monitoring of plants. First, the agile production of high-resolution HMA utilizing low-cost 3D-printing methods has been presented. The fabrication process was optimized by fine-tuning critical parameters, including UV exposure time and layer height, to achieve a tip diameter of 25.9 ± 3.7 µm using a cost-effective 3D printer (<500 EUR). An exposure time of 1.5 seconds and a layer height of 20 µm were identified as the optimal choices for the 3D printing process. Mechanical characterization demonstrated the ability of the 3D-printed HMA to penetrate biological substrates while maintaining its structural integrity. The Parafilm test, simulating insertion into a plant's epidermis, showed robust insertion capabilities, with the 800-µm base design proving to be optimal. The study also assessed the HMA's ability to extract fluid both *in vitro* and *in vivo*. The HMA, when modified with surfactants, demonstrated effective passive fluid extraction from agarose hydrogel and plant leaves, highlighting its potential for sampling plant fluid.

Electrochemical sensing applications were explored for plant health monitoring. The paper-based sampling method, integrated with graphite-based SPEs, provided reliable electrochemical profiling of different plants. The HMAPS effectively sampled plant fluid, and the SPEs, with various modifications, enabled the detection of H_2O_2, glucose, and pH. The method exhibited variations in the analyte levels among different plants, indicating the potential for plant health assessment in diverse contexts. Nevertheless, further testing on plant species and validation with standard methods will be performed to confirm the reliability of the sensing approach.

Integrating 3D-printed HMAs with electrochemical sensing technology offers a promising avenue for rapid, on-site plant health monitoring. Further research must verify its reliability under varying conditions and stress factors. Nonetheless, this technology demonstrates significant potential to enhance our understanding of plant stress monitoring

530 and address the challenges associated with precise farming and crop management in
531 changing climate conditions.
532

533 **CRediT authorship contribution statement**

534 **Marc Parrilla**: Conceptualization, Data curation, Formal analysis, Funding acquisition,
535 Investigation, Methodology, Validation, Visualization, Writing - original draft. **Amadeo**
536 **Sena-Torralba**: Investigation, Methodology, Data curation, Formal analysis, Validation,
537 Visualization, Writing - original draft. **Annemarijn Steijlen**: Investigation,
538 Methodology, Formal analysis, Visualization, Writing - review & editing. **Sergi Morais**:
539 Writing - review & editing. **Ángel Maquieira**: Writing - review & editing. **Karolien De**
540 **Wael**: Writing - review & editing, Resources.

541 **Acknowledgments**

542 M.P. acknowledges the support of the Fund for Scientific Research (FWO) in Flanders
543 (1265223N), Belgium. A.S. acknowledges Generalitat Valenciana and the European
544 Social Fund for the CIAPOS fellowship (CIAPOS/2022/7). S.M. awards grant PID2019-
545 110713RB-I00 funded by MCIN/AEI/ 10.13039/501100011033 and by "ERDF A way of
546 making Europe". The research was financed by the AGROALNEXT/2022/054 grant from
547 Conselleria d'Innovació, Universitats, Ciència i Societat Digital (Generalitat Valenciana,
548 Spain), and MCIN, Next Generation EU (PRTR-C17.I1) funds. The authors acknowledge
549 BOF-UAntwerp and FWO infrastructure funding.

550 **Declaration of interests**

551 The authors have no interests to declare.

552 **References**

553 Aldawood, F.K., Andar, A., Desai, S., 2021. A Comprehensive Review of Microneedles:
554 Types, Materials, Processes, Characterizations and Applications. Polymers (Basel).
555 13, 2815. https://doi.org/10.3390/polym13162815
556 Bukhamsin, A., Ait Lahcen, A., Filho, J.D.O., Shetty, S., Blilou, I., Kosel, J., Salama, K.N.,
557 2022. Minimally-invasive, real-time, non-destructive, species-independent
558 phytohormone biosensor for precision farming. Biosens. Bioelectron. 214,
559 114515. https://doi.org/10.1016/j.bios.2022.114515

560 Chakraborty, S., Newton, A.C., 2011. Climate change, plant diseases and food security:
561 an overview. Plant Pathol. 60, 2–14. https://doi.org/10.1111/j.1365-
562 3059.2010.02411.x
563 Chaloner, T.M., Gurr, S.J., Bebber, D.P., 2021. Plant pathogen infection risk tracks
564 global crop yields under climate change. Nat. Clim. Chang. 11, 710–715.
565 https://doi.org/10.1038/s41558-021-01104-8
566 Chen, Y., Sun, Y., Niu, Y., Wang, B., Zhang, Z., Zeng, L., Li, L., Sun, W., 2023. Portable
567 Electrochemical Sensing of Indole-3-acetic Acid Based on Self-assembled MXene
568 and Multi-walled Carbon Nanotubes Composite Modified Screen-printed
569 Electrode. Electroanalysis 35, 2200279. https://doi.org/10.1002/elan.202200279
570 Coatsworth, P., Gonzalez-Macia, L., Collins, A.S.P., Bozkurt, T., Güder, F., 2022.
571 Continuous monitoring of chemical signals in plants under stress. Nat. Rev. Chem.
572 7, 7–25. https://doi.org/10.1038/s41570-022-00443-0
573 Dabbagh, S.R., Sarabi, M.R., Rahbarghazi, R., Sokullu, E., Yetisen, A.K., Tasoglu, S., 2021.
574 3D-printed microneedles in biomedical applications. iScience 24, 102012.
575 https://doi.org/10.1016/j.isci.2020.102012
576 Detamornrat, U., McAlister, E., Hutton, A.R.J., Larrañeta, E., Donnelly, R.F., 2022. The
577 Role of 3D Printing Technology in Microengineering of Microneedles. Small 18,
578 2106392. https://doi.org/10.1002/smll.202106392
579 Drăgan, A.-M., Parrilla, M., Cambré, S., Domínguez-Robles, J., Detamornrat, U.,
580 Donnelly, R.F., Oprean, R., Cristea, C., De Wael, K., 2023. Microneedle array-based
581 electrochemical sensor functionalized with SWCNTs for the highly sensitive
582 monitoring of MDMA in interstitial fluid. Microchem. J. 193, 109257.
583 https://doi.org/10.1016/j.microc.2023.109257
584 Economidou, S.N., Uddin, M.J., Marques, M.J., Douroumis, D., Sow, W.T., Li, H., Reid,
585 A., Windmill, J.F.C., Podoleanu, A., 2021. A novel 3D printed hollow microneedle
586 microelectromechanical system for controlled, personalized transdermal drug
587 delivery. Addit. Manuf. 38, 101815.
588 https://doi.org/10.1016/j.addma.2020.101815
589 Farvardin, A., González-Hernández, A.I., Llorens, E., García-Agustín, P., Scalschi, L.,
590 Vicedo, B., 2020. The Apoplast: A Key Player in Plant Survival. Antioxidants 9, 604.
591 https://doi.org/10.3390/antiox9070604

592 Friedel, M., Thompson, I.A.P., Kasting, G., Polsky, R., Cunningham, D., Soh, H.T.,
593 Heikenfeld, J., 2023. Opportunities and challenges in the diagnostic utility of
594 dermal interstitial fluid. Nat. Biomed. Eng. https://doi.org/10.1038/s41551-022-
595 00998-9
596 Geilfus, C.M., 2017. The pH of the Apoplast: Dynamic Factor with Functional Impact
597 Under Stress. Mol. Plant 10, 1371–1386.
598 https://doi.org/10.1016/j.molp.2017.09.018
599 Giraldo, J.P., Wu, H., Newkirk, G.M., Kruss, S., 2019. Nanobiotechnology approaches
600 for engineering smart plant sensors. Nat. Nanotechnol. 14, 541–553.
601 https://doi.org/10.1038/s41565-019-0470-6
602 Larrañeta, E., Moore, J., Vicente-Pérez, E.M., González-Vázquez, P., Lutton, R.,
603 Woolfson, A.D., Donnelly, R.F., 2014. A proposed model membrane and test
604 method for microneedle insertion studies. Int. J. Pharm. 472, 65–73.
605 https://doi.org/10.1016/j.ijpharm.2014.05.042
606 Lee, G., Wei, Q., Zhu, Y., 2021. Emerging Wearable Sensors for Plant Health
607 Monitoring. Adv. Funct. Mater. 31, 2106475.
608 https://doi.org/10.1002/adfm.202106475
609 Lesk, C., Rowhani, P., Ramankutty, N., 2016. Influence of extreme weather disasters on
610 global crop production. Nature 529, 84–87. https://doi.org/10.1038/nature16467
611 Li, Z., Yu, T., Paul, R., Fan, J., Yang, Y., Wei, Q., 2020. Agricultural nanodiagnostics for
612 plant diseases: Recent advances and challenges. Nanoscale Adv. 2, 3083–3094.
613 https://doi.org/10.1039/c9na00724e
614 Lima, A.S., Prieto, K.R., Santos, C.S., Paula Valerio, H., Garcia-Ochoa, E.Y., Huerta-
615 Robles, A., Beltran-Garcia, M.J., Di Mascio, P., Bertotti, M., 2018. In-vivo
616 electrochemical monitoring of H2O2 production induced by root-inoculated
617 endophytic bacteria in Agave tequilana leaves. Biosens. Bioelectron. 99, 108–114.
618 https://doi.org/10.1016/j.bios.2017.07.039
619 Lo Presti, D., Di Tocco, J., Massaroni, C., Cimini, S., De Gara, L., Singh, S., Raucci, A.,
620 Manganiello, G., Woo, S.L., Schena, E., Cinti, S., 2023. Current understanding,
621 challenges and perspective on portable systems applied to plant monitoring and
622 precision agriculture. Biosens. Bioelectron. 222, 115005.
623 https://doi.org/10.1016/j.bios.2022.115005

624 Lowenberg-Deboer, J., Erickson, B., 2019. Setting the record straight on precision
625 agriculture adoption. Agron. J. 111, 1552–1569.
626 https://doi.org/10.2134/agronj2018.12.0779
627 Mathew, E., Pitzanti, G., Gomes dos Santos, A.L., Lamprou, D.A., 2021. Optimization of
628 Printing Parameters for Digital Light Processing 3D Printing of Hollow Microneedle
629 Arrays. Pharmaceutics 13, 1837. https://doi.org/10.3390/pharmaceutics13111837
630 Mohammad-Razdari, A., Rousseau, D., Bakhshipour, A., Taylor, S., Poveda, J., Kiani, H.,
631 2022. Recent advances in E-monitoring of plant diseases. Biosens. Bioelectron.
632 201, 113953. https://doi.org/10.1016/j.bios.2021.113953
633 Mounesh, N., Manikanta, P., Reddy, K.R.V., Selvaraj, M., Vidyasagar, C.C., Nagaraja,
634 B.M., 2023a. Novel decorated aluminium(iii) phthalocyanine complex with the
635 application of MWCNTs on electrodes: electrochemical non-enzymatic oxidation
636 and reduction of glucose and hydrogen peroxide. RSC Adv. 13, 20723–20736.
637 https://doi.org/10.1039/d3ra02617e
638 Mounesh, N., Manriquez, J.M., Venugopala Reddy, K.R., Shilpa, K.G., Nagaraja, B.M.,
639 2023b. Electrochemical, Ultrasensitive, and Selective Detection of Nitrite and
640 H2O2: Novel Macrostructured Phthalocyanine with Composite MWCNTs on a
641 Modified GCE. Langmuir 39, 1665–1676.
642 https://doi.org/10.1021/acs.langmuir.2c03202
643 Nassar, J.M., Khan, S.M., Villalva, D.R., Nour, M.M., Almuslem, A.S., Hussain, M.M.,
644 2018. Compliant plant wearables for localized microclimate and plant growth
645 monitoring. Flex. Electron. 2, 24. https://doi.org/10.1038/s41528-018-0039-8
646 Parrilla, M., Detamornrat, U., Domínguez-Robles, J., Donnelly, R.F., De Wael, K., 2022a.
647 Wearable Hollow Microneedle Sensing Patches for the Transdermal
648 Electrochemical Monitoring of Glucose. Talanta 249, 123695.
649 https://doi.org/10.1016/j.talanta.2022.123695
650 Parrilla, M., Detamornrat, U., Domínguez-Robles, J., Tunca, S., Donnelly, R.F., De Wael,
651 K., 2023a. Wearable Microneedle-Based Array Patches for Continuous
652 Electrochemical Monitoring and Drug Delivery: Toward a Closed-Loop System for
653 Methotrexate Treatment. ACS Sensors 8, 4161–4170.
654 https://doi.org/10.1021/acssensors.3c01381
655 Parrilla, M., Slosse, A., Echelpoel, R. Van, Montiel, N.F., Langley, A.R., Durme, F. Van,

656 Wael, K. De, 2022b. Rapid On-Site Detection of Illicit Drugs in Smuggled Samples
657 with a Portable Electrochemical Device. Chemosensors 10, 108.
658 https://doi.org/10.3390/chemosensors10030108
659 Parrilla, M., Vanhooydonck, A., Johns, M., Watts, R., Wael, K. De, 2023b. 3D-printed
660 microneedle-based potentiometric sensor for pH monitoring in skin interstitial
661 fluid. Sensors Actuators B. Chem. 378, 133159.
662 https://doi.org/10.1016/j.snb.2022.133159
663 Radoglou-Grammatikis, P., Sarigiannidis, P., Lagkas, T., Moscholios, I., 2020. A
664 compilation of UAV applications for precision agriculture. Comput. Networks 172,
665 107148. https://doi.org/10.1016/j.comnet.2020.107148
666 Saifullah, K.M., Faraji Rad, Z., 2023. Sampling Dermal Interstitial Fluid Using
667 Microneedles: A Review of Recent Developments in Sampling Methods and
668 Microneedle-Based Biosensors. Adv. Mater. Interfaces 10, 2201763.
669 https://doi.org/10.1002/admi.202201763
670 Shahrubudin, N., Lee, T.C., Ramlan, R., 2019. An overview on 3D printing technology:
671 Technological, materials, and applications. Procedia Manuf. 35, 1286–1296.
672 https://doi.org/10.1016/j.promfg.2019.06.089
673 Shao, B., Ai, Y., Yan, L., Wang, B., Huang, Y., Zou, Q., Fu, H., Niu, X., Sun, W., 2023.
674 Wireless electrochemical sensor for the detection of phytoregulator indole-3-
675 acetic acid using gold nanoparticles and three-dimensional reduced graphene
676 oxide modified screen printed carbon electrode. Talanta 253, 124030.
677 https://doi.org/10.1016/j.talanta.2022.124030
678 Singh, B.K., Delgado-Baquerizo, M., Egidi, E., Guirado, E., Leach, J.E., Liu, H., Trivedi, P.,
679 2023. Climate change impacts on plant pathogens, food security and paths
680 forward. Nat. Rev. Microbiol. 21, 640–656. https://doi.org/10.1038/s41579-023-
681 00900-7
682 Steijlen, A.S.M., Parrilla, M., Van Echelpoel, R., De Wael, K., 2024. Dual Microfluidic
683 Sensor System for Enriched Electrochemical Profiling and Identification of Illicit
684 Drugs On-Site. Anal. Chem. 96, 590–598.
685 https://doi.org/10.1021/acs.analchem.3c05039
686 Uddin, M.J., Scoutaris, N., Economidou, S.N., Giraud, C., Chowdhry, B.Z., Donnelly, R.F.,
687 Douroumis, D., 2020. 3D printed microneedles for anticancer therapy of skin

tumours. Mater. Sci. Eng. C 107, 110248. https://doi.org/10.1016/j.msec.2019.110248

Wang, H.R., Bi, X.M., Fang, Z.J., Yang, H., Gu, H.Y., Sun, L.J., Bao, N., 2019. Real time sensing of salicylic acid in infected tomato leaves using carbon tape electrodes modified with handed pencil trace. Sensors Actuators, B Chem. 286, 104–110. https://doi.org/10.1016/j.snb.2019.01.119

Wang, Z., Xue, L., Li, M., Li, C., Li, P., Li, H., 2021. Au@SnO2-vertical graphene-based microneedle sensor for in-situ determination of abscisic acid in plants. Mater. Sci. Eng. C 127, 112237. https://doi.org/10.1016/j.msec.2021.112237

Xenikakis, I., Tzimtzimis, M., Tsongas, K., Andreadis, D., Demiri, E., Tzetzis, D., Fatouros, D.G., 2019. Fabrication and finite element analysis of stereolithographic 3D printed microneedles for transdermal delivery of model dyes across human skin in vitro. Eur. J. Pharm. Sci. 137, 104976. https://doi.org/10.1016/j.ejps.2019.104976

Yu, T., Zhang, X., Gao, S., Cao, M., Lei, X., Yang, Y., Liu, Y., Zhu, L., Tian, B., Gu, H., Li, Y., 2022. Tobacco Growth Monitoring and Variety Identification Based on Electrochemical Fingerprints. Int. J. Electrochem. Sci. 17, 22089. https://doi.org/10.20964/2022.08.14

Zhu, D.D., Zheng, L.W., Duong, P.K., Cheah, R.H., Liu, X.Y., Wong, J.R., Wang, W.J., Tien Guan, S.T., Zheng, X.T., Chen, P., 2022. Colorimetric microneedle patches for multiplexed transdermal detection of metabolites. Biosens. Bioelectron. 212, 114412. https://doi.org/10.1016/j.bios.2022.114412

720 **Graphical abstract**

721